ADVANCED MATERIALS
www.advmat.de

Highly Ordered Eutectic Mesostructures via Template-Directed Solidification within Thermally Engineered Templates

Sung Bum Kang, Guanglong Huang, Gaurav Singhal, Dajie Xie, Daniel H. Hsieh, Youngmun Lee, Ashish A. Kulkarni, John W. Smith, Qian Chen, Katsuyo Thornton, Sanjiv Sinha, and Paul V. Braun**

Template-directed self-assembly of solidifying eutectics results in emergence of unique microstructures due to diffusion constraints and thermal gradients imposed by the template. Here, the importance of selecting the template material based on its conductivity to control heat transfer between the template and the solidifying eutectic, and thus the thermal gradients near the solidification front, is demonstrated. Simulations elucidate the relationship between the thermal properties of the eutectic and template and the resultant microstructure. The overarching finding is that templates with low thermal conductivities are generally advantageous for forming highly organized microstructures. When electrochemically porosified silicon pillars (thermal conductivity < 0.3 $Wm^{-1}K^{-1}$) are used as the template into which an AgCl-KCl eutectic is solidified, 99% of the unit cells in the solidified structure exhibit the same pattern. In contrast, when higher thermal conductivity crystalline silicon pillars ($\approx$100 $Wm^{-1}K^{-1}$) are utilized, the expected pattern is only present in 50% of the unit cells. The thermally engineered template results in mesostructures with tunable optical properties and reflectances nearly identical to the simulated reflectances of perfect structures, indicating highly ordered patterns are formed over large areas. This work highlights the importance of controlling heat flows in template-directed self-assembly of eutectics.

1. Introduction

Template-directed self-assembly utilizes a predefined template to drive formation of microstructures not naturally present in the native self-assembling system and to enhance both the short and long-range order of the resultant microstructure.[1–4] Order is particularly important as many proposed applications for self-assembled materials are incompatible with the defects prevalent in conventionally self-assembled materials.[5–7] A high degree of order can result in materials with improved mechanical strength,[8] magnetic properties,[9] useful optical properties,[10] and highly anisotropic electrical conductivity.[11] However, achieving order through self-assembly is a significant challenge due to instabilities that arise during the self-assembly process, which lead to defects in the resultant mesostructure.[12–15]

While much work on self-assembly has focused on polymeric and colloidal systems, we have chosen to concentrate on inorganic self-assembly, and in particular

S. B. Kang, G. Singhal, D. Xie, J. W. Smith, Q. Chen, P. V. Braun
Department of Materials Science and Engineering
University of Illinois
Urbana, IL 61801, USA
E-mail: pbraun@illinois.edu

S. B. Kang, G. Singhal, D. Xie, J. W. Smith, Q. Chen, P. V. Braun
Materials Research Laboratory
University of Illinois
Urbana, IL 61801, USA

The ORCID identification number(s) for the author(s) of this article can be found under https://doi.org/10.1002/adma.202308720

DOI: 10.1002/adma.202308720

G. Huang, K. Thornton
Department of Materials Science and Engineering
University of Michigan
Ann Arbor, MI 48109, USA
E-mail: kthorn@umich.edu

D. H. Hsieh, Y. Lee, S. Sinha, P. V. Braun
Department of Mechanical Science and Engineering
University of Illinois
Urbana, IL 61801, USA

A. A. Kulkarni
Center for Functional Nanomaterials
Brookhaven National Laboratory
Upton, NY 11973, USA

Q. Chen, P. V. Braun
Department of Chemical and Biomolecular Engineering
University of Illinois
Urbana, IL 61801, USA

inorganic eutectic alloys.[16,17] This choice is motivated by the fact that inorganic eutectics have been shown to exhibit unique surface and bulk plasmonic properties,[18-20] attractive catalytic properties,[21] and generate microstructures of interest for electrochemical energy storage,[22] while offering manufacturing advantages due to their lowered melting points.[23] All eutectic materials (organic and inorganic) solidify from a homogeneous liquid to two or more distinct solid phases upon cooling. The resultant microstructure is determined by not only the chemistry of the specific system, but also the solidification conditions, latter of which can be controlled externally and provides a wide range of parameter space to be explored. For example, Choi et al. showed in one system that as the solidification rate increased, the microstructure evolved from rod-like to lamellar,[24] and Perrut et al. showed that if the isotherm became curved during solidification that long-range symmetry in the eutectic pattern is lost, leading to localized structures of various form emerging in the solidified eutectic.[25, 26]

As these and other reports have shown, thermal fluctuations can significantly affect the microstructure of a solidifying eutectic.[17,27,28] As temperature fluctuates spatially and temporally, the growth rate of the solid at a region can become faster than other regions, causing changes in the eutectic mesostructure (e.g., the spacing or size of eutectic rods or lamellas), which in turn affects the properties of the resulting solid.[29,30] When these fluctuations are present there can be morphological transitions (e.g., lamellar to rod-like),[31,32] and in some cases there is even complete breakup of the periodic mesostructure, leading to disordered patterns.[27]

As already mentioned, a key motivation to apply a template to a self-assembling material is to guide the self-assembling structure to exhibit long-range periodicity. Another motivation is that the template can even lead to the emergence of mesostructures that cannot otherwise be formed.[16,28-30] In our previous work on templated eutectic solidification, we observed some level of long-range periodicity and the emergence of new mesostructures. However, we also often observed destabilization of the solidification front and microstructures that were often only locally ordered.[16,28] Through the present work, we find that the solidification front is destabilized due to the high thermal conductivity of the pillars (thermal conductivity, $\kappa = 90.7\ \mathrm{Wm^{-1}K^{-1}}$) comprising the template. Thus, we here focus on the impacts of the thermal properties of the template and solidifying/solidified materials on heat transfer in the sample during solidification and demonstrate how template thermal properties play a critical role in determining the regularity of the resultant mesostructure. Specifically, we use templates with significantly smaller κ than the eutectic liquid and the resultant solid phases and find that low κ templates results in unique, highly regular microstructures with long-range order. The template is specifically comprised of porous silicon (pSi) ($\kappa_{pSi} \approx 0.28\ \mathrm{Wm^{-1}K^{-1}}$) formed through electrochemical porosification of crystalline Si ($\kappa_{Si} \approx 96\ \mathrm{Wm^{-1}K^{-1}}$). Simulations demonstrate that the template's low thermal conductivity is key in establishing a vertical temperature gradient during solidification and minimizing thermal gradients in directions perpendicular to the primary solidification direction.

Furthermore, by selective etching of one of the phases present in the self-assembled eutectic and/or the template, microstructures with a range of optical properties are formed. We show how even small variations in the eutectic mesostructure's periodicity can significantly diminish the optical properties of the material, highlighting the importance of template thermal engineering to drive the formation of precisely controlled mesostructures.

2. Results and Discussion

2.1. The Effect of the Template Symmetry on Eutectic Microstructure

As in our initial work on template-directed eutectic solidification, we utilize the lamellae/rod AgCl-KCl eutectic system.[16,28] In this section, we further examine the template geometry and solidification conditions that induce a diversity of patterns. As expected, depending on the processing conditions that lead to different rates of solidification, the resulting solidified eutectic undergoes morphological transitions.[24] In the absence of a template, the bulk AgCl-KCl eutectic melt typically solidifies into one of two microstructures: a lamellar structure consisting of alternating layers of AgCl and KCl at faster solidification rates and a rod-like microstructure consisting of rods of KCl in a AgCl matrix at slower solidification rates. At intermediate solidification rates, a mixture of the two can appear. We confirm the chemical composition of the microstructures by Energy Dispersive X-Ray Spectroscopy (EDS) (Figure S1a,b, Supporting Information). For both the lamellar (Figure S2a–d, Supporting Information) and rod patterns (Figure S2f–h, Supporting Information), the eutectic spacing (λ) decreases as the rate of solidification increases, as expected (summarized in Figure S2, Supporting Information). The rate of solidification is controlled as described in the Experimental section.

When eutectic solidification is carried out within Si pillar templates as illustrated in Figure S3 (Supporting Information) and **Figure 1a**, the diffusion landscape in the liquid ahead of the solidification front is perturbed by the template geometry (the pillars serve as no-flux boundaries for chemical diffusion) resulting in new morphologies distinct from both the starting eutectic pattern and the template.[16] When the rate of solidification is such that AgCl-KCl forms a lamellar pattern (faster solidification rates), the pillar-template-directed eutectic solidification results in Archimedean lattices when the pillars are on a hexagonal array (Figure 1b,c). When the pillars are arranged in a square lattice, chain patterns emerge (Figure 1d,e), consisting of spokes locally veered toward pillars. Both the observed Archimedean and chain patterns correspond well to patterns predicted by phase field simulations that were performed in advance of experiments[16,28,33] (Figures S4 and S5, Supporting Information). When the conditions are such that the bulk eutectic forms a rod-like microstructure (slower solidification rates), solidification within a

Q. Chen, P. V. Braun
Department of Chemistry
University of Illinois
Urbana, IL 61801, USA
Q. Chen, P. V. Braun
Beckman Institute for Advanced Science and Technology
University of Illinois
Urbana, IL 61801, USA

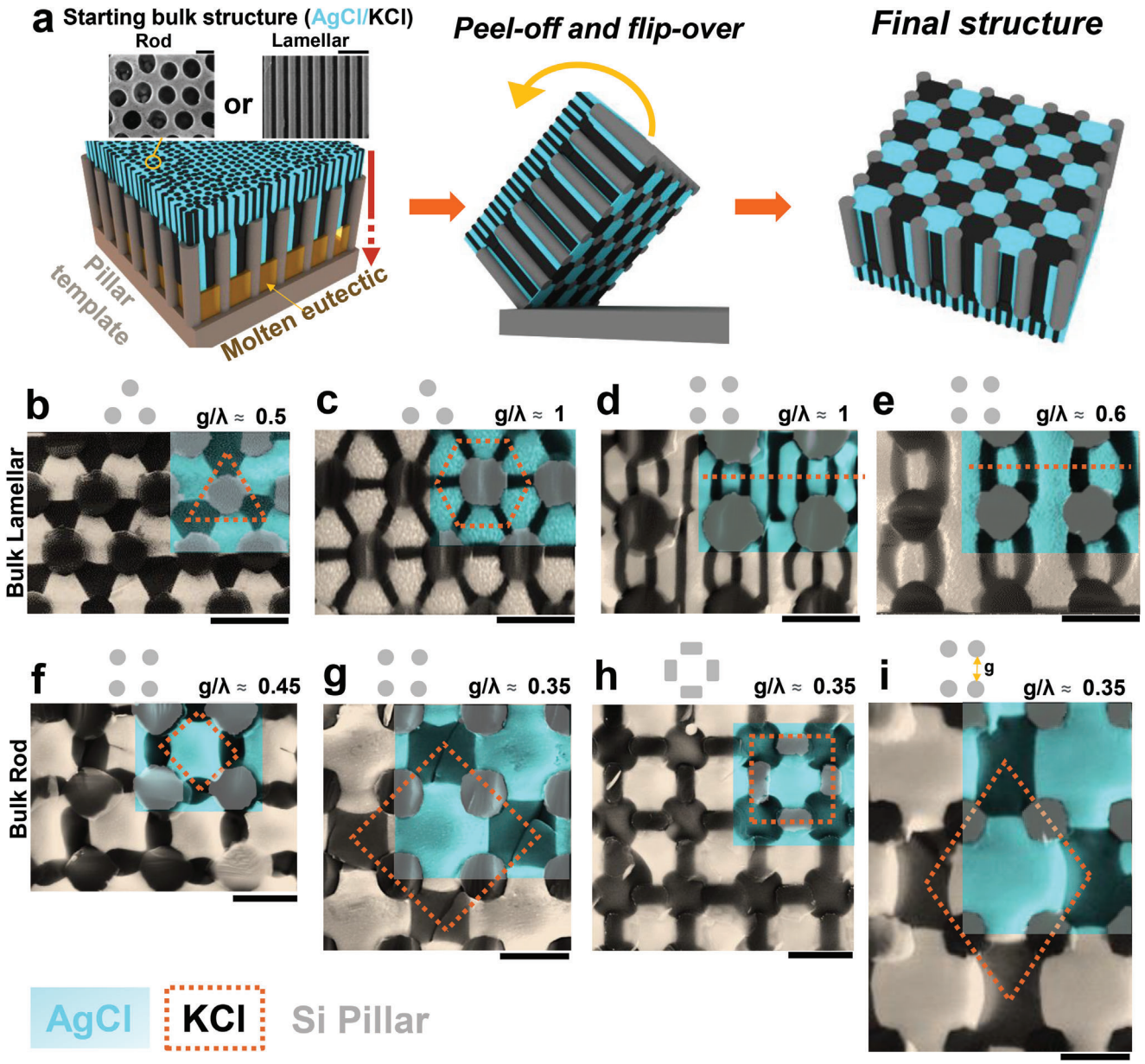

Figure 1. Emerging patterns in template-directed eutectic solidification. a) Schematic illustration of the template-directed eutectic solidification process. The molten (yellow) AgCl (cyan)-KCl (black) binary eutectic directionally solidifies through a pillar template. The solidification direction is along the red arrow, which is aligned with the axis of the Si pillars. The solidified patterns at the interface between the substrate and the template/eutectic system are exposed by peeling off the pillars and solidified eutectic from the substrate. b-i) SEM images of patterns obtained by controlling the solidification rate and template geometries. The orange dotted box is added to illustrate the symmetry of the KCl regions (vertices of the box) of the structure: b,c) Archimedean lattices (triangular template lattice), d,e) chain-shaped patterns, f) cross patterns (the cross is formed by KCl arms with a template pillar in the center), g) checkerboard patterns, h) inverse cross patterns (the cross consists of arms if the rectangular pillars connected with a KCl rod in the center), i) elongated checkerboard pattern formed by a rectangular template lattice. The template pattern for d-h is a square lattice. All scale bars are 3 µm. Included above each SEM image is the value of g/λ and the symmetry of the template depicted with gray dots/rectangles. Except as indicated in (i), g is the gap spacing between nearest neighbor pillars. The bulk eutectic structure is lamellar for (b-e) and rod-like for (f-i). Si templates are used in these samples.

square-lattice of pillar template results in cross and checkerboard patterns. The eutectic spacing as well as pillar distance are key parameters that determine the observed patterns, as summarized in a morphological phase map that includes detailed SEM images (Figure S6, Supporting Information). In the cross pattern (Figure 1f), KCl solidifies into spokes and AgCl into squares between the pillars. In checkerboard patterns (Figure 1g), AgCl and KCl form squares alternating in both directions. It is important to note that a wider variety of patterns can be realized if the shape of the pillar is modified. For example, when utilizing

rectangular pillars (Figure S7, Supporting Information) instead of circular pillars, the cross pattern can be modified such that KCl forms a more circular shape while the AgCl remains in the same position with only a slight change in the morphology as compared to the circular-pillar template (cf. Figure 1h,f). If the square lattice of the pillars is modified into a rectangular lattice, the pattern is further modified. For instance, the rectangular template pattern leads to an elongated-checkerboard pattern of the solidified eutectic, where AgCl remains square while KCl forms into rectangles (Figure 1i). While we have only investigated a small subset of potential template structures, its clear modifications of the template provide considerable tunability in designing the resultant eutectic microstructures.

2.2. Impact of Template Thermal Properties

Along with template geometry, template thermal properties play a critical role in controlling pattern formation. If considerable heat flows through the template, the solidification front can become curved or slanted,[25,26,30] and solidification is no longer unidirectional. The shape of the solidification front can be estimated from the temperature field by the isothermal contour or surface (depending on the dimension) at the eutectic temperature; in the absence of supersaturation, the solidification front is well approximated by this contour/surface.[25,30] The direction of thermal gradients at the solidification front, which is related to the isotherm at the eutectic temperature, dictates the direction of solidification. The thermal gradient can include temperature gradients along both the vertical and horizontal axes. The vertical gradient (z-axis) is parallel to the direction of the externally applied temperature gradient, while gradients in the horizontal directions (x-axis) are due to local perturbations in the temperature field created by the template (**Figure 2**a; Figure S8a, Supporting Information). Thermal gradients in the horizontal directions tend to induce irregularity in pattern formations,[16] and thus they should be minimized. When the pillars have a high thermal conductivity ($\kappa_{template}$ = 110 $Wm^{-1}K^{-1}$), a highly curved isothermal surface is observed (the red curve in Figure S8b, Supporting Information),[34] and thermal gradients in the horizontal directions are considerable, especially near the eutectic/template interface. The isothermal surface remains curved (Figure S8c, Supporting Information) even at a conductivity of ≈10 $Wm^{-1}K^{-1}$ (lower than the lowest plausible thermal conductivity of the silicon pillars taking into account the confinement and thermal effects[35]). However, once the template thermal conductivity is significantly lower (e.g., $\kappa_{template} \approx 1$ $Wm^{-1}K^{-1}$), the isothermal surface at the eutectic temperature becomes essentially flat (Figure S8d, Supporting Information), which indicates that the temperature gradient is essentially vertical. Figure 2b quantifies the relationship between the thermal gradient at the solidification front and the thermal conductivity of the eutectic material and the template in terms of an alignment ratio. The alignment ratio, the ratio of the vertical component of the thermal gradient to the total magnitude of the thermal gradient, illustrates how the thermal gradient at the solidification front aligns with the direction of solidification. For example, an alignment ratio of 1.0 indicates a thermal gradient that is oriented in the vertical direction. When the vertical and horizontal thermal gradients are approximately equal in magnitude ($|\nabla T_{Vertical}| \approx |\nabla T_{Horizontal}|$), the alignment ratio ($|\nabla T_{Vertical}| / |\nabla T|$) is $1/\sqrt{2} \approx 0.714$. The template with low thermal conductivity consistently exhibits an alignment ratio near 1.0 across the entire range of template and eutectic thermal conductivity values. It is worth noting that when the thermal conductivity of the eutectic materials matches that of the template, the thermal gradient also remains predominantly vertical. Since achieving an exact match in thermal conductivity is challenging,[36-39] a thermal insulating template provides a more practical solution for maintaining a predominantly vertical thermal gradient. Within a thermal insulating template, the horizontal component of the thermal gradient (taken here as the x component, as described in Figure 2a) remains small throughout the vertical axial span of the pillar, from the upper (pillar top) to the lower (pillar bottom) end of the pillar (blue curve, Figure 2c), in contrast to the high thermal conductivity template where the horizontal component of the thermal gradient is significant (red curve, Figure 2c). As illustrated in Figure 2d and e, in case of a thermally conductive template ($\kappa_{template}$ = 110 $Wm^{-1}K^{-1}$), the solidification front starts out planar in the bulk (as expected) until it is just above the template. Upon entering the template, the temperature gradients become strongly curved (Figure 2d-(0 µm). At the middle of the pillar, the isothermal contour plane reverts to flat (Figure 2d, 5 µm). Upon approaching the bottom of the template, the solidification-front curvature increases, (Figure 2d, 10 µm). We contrast this with the isothermal eutectic temperature surfaces in a lower thermal conductivity pillar template ($\kappa_{template} \approx 1$ $Wm^{-1}K^{-1}$), which remain flat as the solidification front propagates through the template (Figure 2e).

To provide input parameters for the heat transfer simulations, we quantify the thermal properties of the Si and pSi templates. Si pillar arrays were created by photolithography followed by deep reactive ion etching (**Figure 3**a). To form pSi pillars, these Si pillars are electrochemically porosified, drastically decreasing their κ and volumetric heat capacity (ρC_p).[40-43] As we previously showed, Si pillars can be completely porosified via such a process.[44] See Experimental section for details. As shown in Figure 3b and Figure S9 (Supporting Information), even after electrochemical porosification, the integrity of the pillar template is maintained. While we cannot directly measure κ and ρC_p of the pillars, we measure κ and ρC_p of the starting silicon and a pSi layer, providing an upper bound to κ and ρC_p of the pSi pillars. Using the 3-omega method (details in Experimental section and Supporting Information), as shown in Figure 3c, the slope of the line fitted to the amplitude of temperature oscillations with respect to frequency of heating from a metal line yields κ_{Si} of 96 $Wm^{-1}K^{-1}$. The Si is single-crystal and boron-doped to ≈10^{19} cm^{-3}, making 96 $Wm^{-1}K^{-1}$ reasonable since doping reduces κ.[45] After porosification, κ of pSi is 0.28 $Wm^{-1}K^{-1}$ (details in Supporting Information). The reduced κ of pSi is both due to removal of material and thermal phonon scattering by the porous structure.[41] The heat capacities of bulk Si and pSi are measured using differential scanning calorimetry (DSC). Using the estimated porosity of pSi (≈81%, as deduced from the effective medium theory and shown in Figure S10, Supporting Information), the volumetric heat capacity as a function of temperature is determined (Figure 3d). The volumetric heat capacity values obtained are 1.68 MJ $m^{-3}K$ for Si and

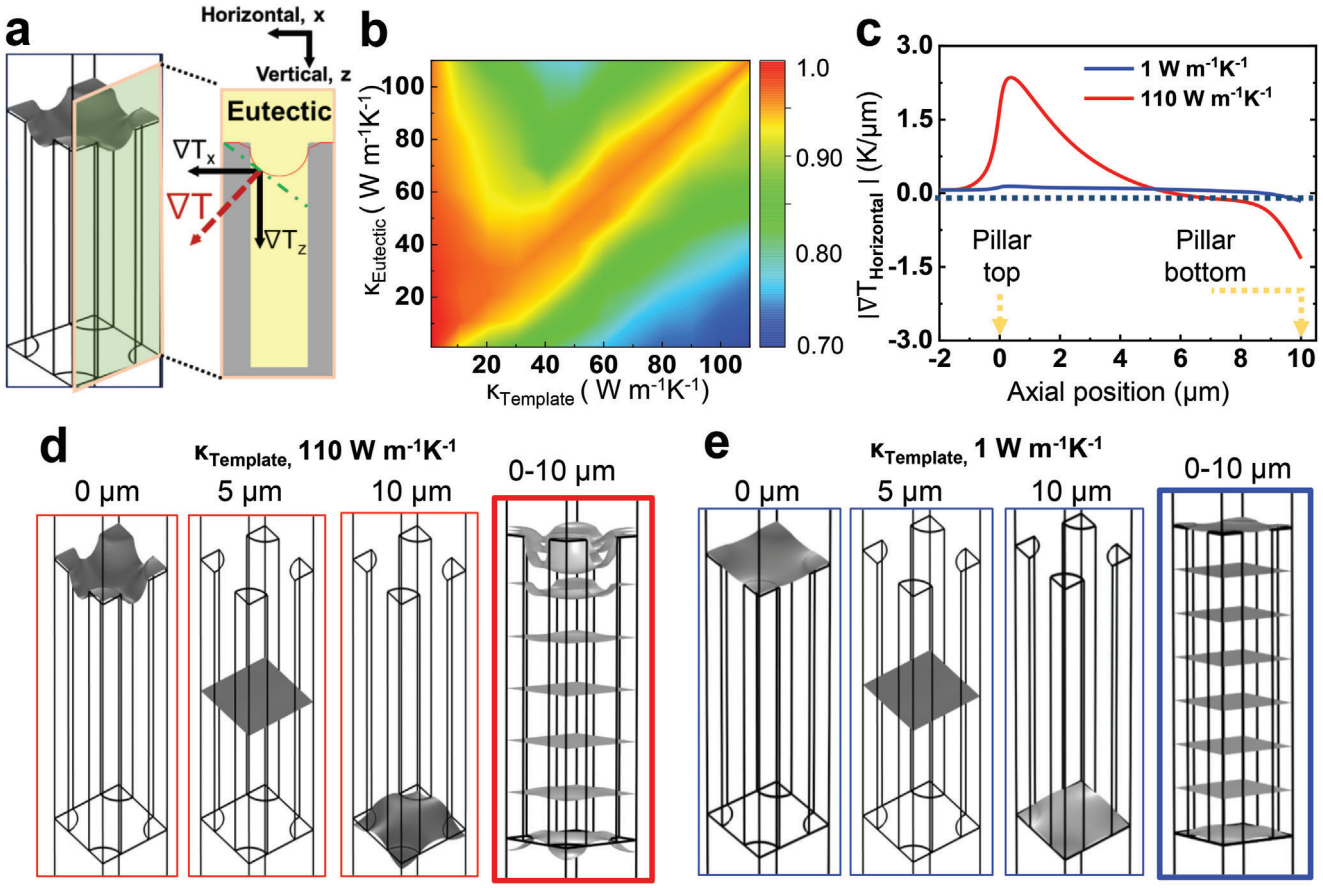

Figure 2. Time-dependent simulation of temperature evolution during template-directed solidification. a) The 3D isothermal surface plot (left) was transformed into a 2D representation through a cross section connecting the centers of the first nearest pillars. Right is a schematic illustration with the isotherm at eutectic temperature indicated by a thin red curve. The thermal gradient is calculated at the surface having the eutectic temperature and, in general, possesses both vertical and horizontal components. The vertical direction represents the direction of the externally applied thermal gradient, while the horizontal directions include all directions perpendicular to the vertical direction. b) The alignment ratio of the thermal gradient, the ratio of the magnitude of the vertical component of the thermal gradient ($|\nabla T_{Vertical}|$) to the magnitude of thermal gradient ($|\nabla T|$), measured at ¼ of the inter-pillar spacing from the interface, as a function of the thermal conductivity of the eutectic and template components (ranging from 1 $Wm^{-1}K^{-1}$ to 110 $Wm^{-1}K^{-1}$). c) The magnitude of the horizontal component of the thermal gradient, measured in the x direction in the plane shown with the green shade in (a) at ¼ of the inter-pillar spacing from the interface, versus z position as defined in (a) with 0 μm corresponding to the top of the pillars (the interface between the bulk eutectic and the template) and 10 μm as the bottom of the pillars. Blue line: low thermal conductivity template, 1 $Wm^{-1}K^{-1}$. Red line: high thermal conductivity template, 110 $Wm^{-1}K^{-1}$). Isothermal contour plot (at eutectic temperature (T = 591.73 K)) at each axial position of d) the high thermal conductivity template (110 $Wm^{-1}K^{-1}$), and e) the low thermal conductivity template (1 $Wm^{-1}K^{-1}$), at 0, 5, and 10 μm as defined in (c). Also shown is a stack of the isothermal surfaces at the solidification front during solidification from the top to the bottom of the pillar template (right images in d and e within the thicker red/blue boxes).

0.249 MJ $m^{-3}K$ for pSi. We also calculate the thermal diffusivity (given by $\kappa/\rho C_p$); We find that the thermal diffusivity of pSi is 65 times and 23 times lower than that of Si and Ni, respectively (as illustrated in Figure 3e), indicating much less heat will flow from the solidifying eutectic into the pSi template. We note that thermal diffusivity, in addition to thermal conductivity, is an important property to consider in characterizing the heat transfer during solidification because thermal diffusivity governs the evolution of the temperature profile and thus the gradient. The temperature profile and thermal gradient in turn changes the solidification front morphology and speed, which have a direct impact on the resultant eutectic structure.[46-49] On the other hand, thermal conductivity dictates the path of the heat flow when multiple materials with different conductivities are present. If one material has a much higher conductivity, heat will be transported predominantly by that material. The low thermal diffusivity and thermal conductivity of the template results in the template serving both as a thermal and chemical no-flux boundary, in contrast to when Si and Ni are used as the template materials, in which case the template provides only a chemical no-flux boundary.

2.3. Quantification of Template-Directed 3D Order

An AgCl-KCl eutectic directionally solidified in the Si pillar template generally results in a checkerboard pattern when the eutectic forms a rod microstructure in the absence of a template,

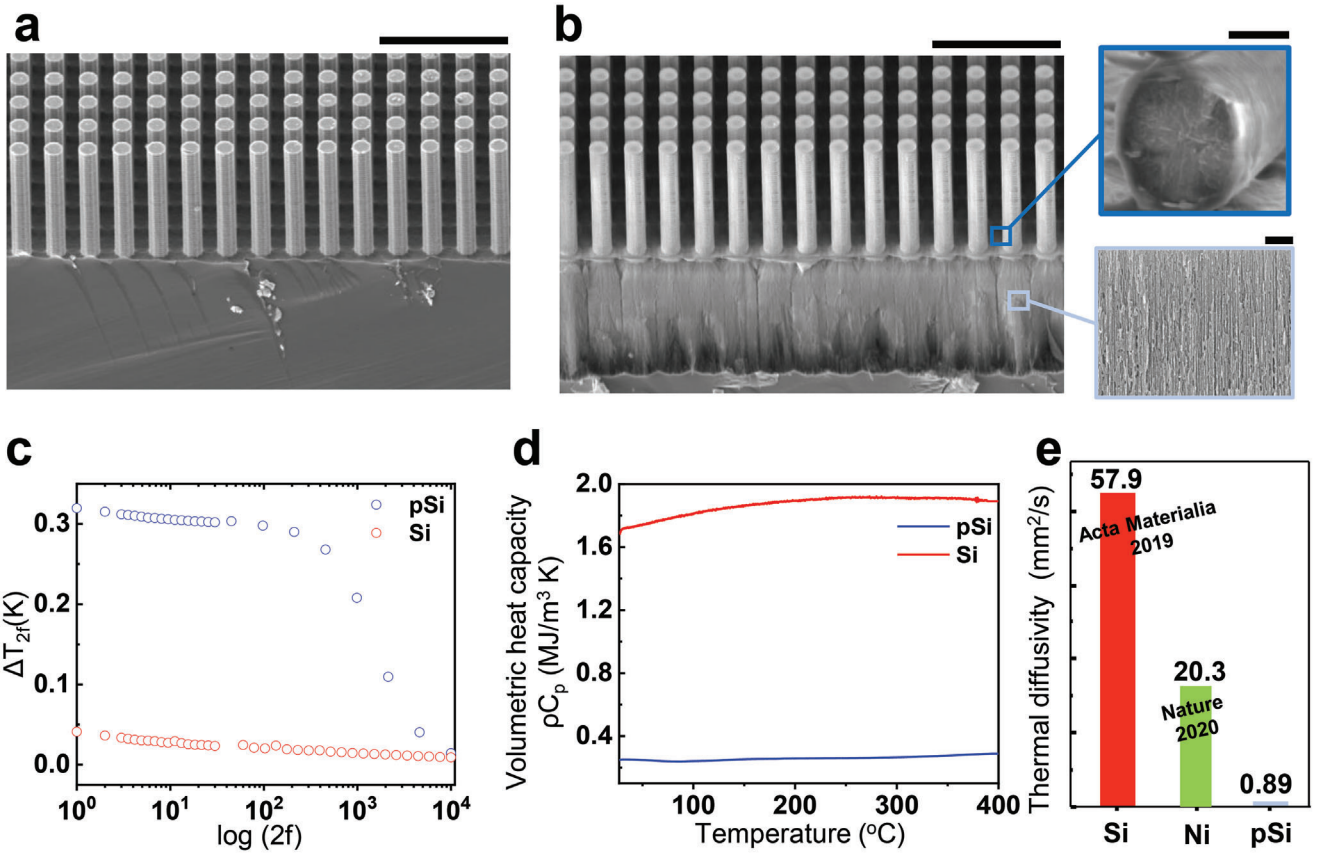

Figure 3. Thermal properties of templates. a,b) SEM images of templates used for eutectic solidification. a) Si pillar array (scale bar: 10 μm), b) pSi pillar array (scale bar: 10 μm), cross-section of pSi pilar and high magnification image of pSi (scale bar: 1 μm). c) Temperature oscillations across pSi (blue circles) and Si (red circles) as function of frequency. d) Volumetric heat capacity of pSi (blue line) and Si (red line) as function of temperature. e) Thermal diffusivity of previously employed (Si, Ni)[16,25] and current (pSi) template materials.

as seen in **Figure** 4a. However, as discussed earlier, the non-planar solidification front, along with non-uniform solidification rate, results in variation in the solidification conditions across the microstructure. Quantitative image analysis of the surface shows considerable deviations from the checkerboard pattern, providing evidence for such variation. Out of 104 unit cells, only 49% exhibit the checkerboard pattern (Figure 4b). The remaining unit cells have various defects. On the other hand, 99% of the unit cells exhibited the checkerboard structure when the pSi pillar template was employed, with all other conditions held the same as above (Figure 4c,d). Such long-range ordering of the checkerboard patterns can be attributed to the low thermal diffusivity of the pillar template that promotes a flat isothermal surface during eutectic solidification. The SEM image showing the structures perpendicular to the substrate (parallel to the pillars) is obtained using focused-ion-beam (FIB) milling (Figure 4e,f). Top-view SEM images (showing the structure in the plane parallel to the substrate) from top (vi) to bottom (i) are generated through a series of ion-milling steps (Figure 4g,h); more details are provided below. The heights indicated in Figure 3e,f correspond to the levels marked as (vi to i) in Figure 4g,h. In the cross-sectional images of the templated region of the Si pillar template system, a disordered microstructure is observed, indicating thermal fluctuations are present during solidification (Figure 4e). In contrast, the cross section of the checkerboard pattern formed in the pSi template system shows a clear alternating microstructure of AgCl and KCl (Figure 4f), in agreement with the long-range order in the checkerboard pattern (Figure 4c).

A sequence of ion-milling steps is specifically designed to build a 3D map of the templated structures. In brief, the same region of a sample is etched stepwise top-down via argon ion beam milling (details in Experimental section) with the etch depth of each step precisely controlled by time and etch power (Figure S11, Supporting Information). A SEM image is taken after each ≈2.5 μm etching step. Figure 4g shows serial sectioning SEM images of the checkerboard patterns formed in the Si template system at depths of −2.5 μm (in the bulk eutectic), 0 μm (set at the top side of the pillar that corresponds to the interface between the bulk eutectic and the template), 2.5, 5.0, 7.5, and 10 μm (at the template/substrate interface, where solidification ends). These cross-sectional images show multiple transitions between rod and lamellar, alternating between spoke and checkerboard patterns (Figure 4g; see Figure S12a, Supporting Information). The initial bulk eutectic rod structure (Figure 4gi) transitioned to a lamellar structure at the top of the template (Figure 4gii). The lamellar structure then changes to form spoke patterns due to the presence of template (Figure 4giii,iv) and

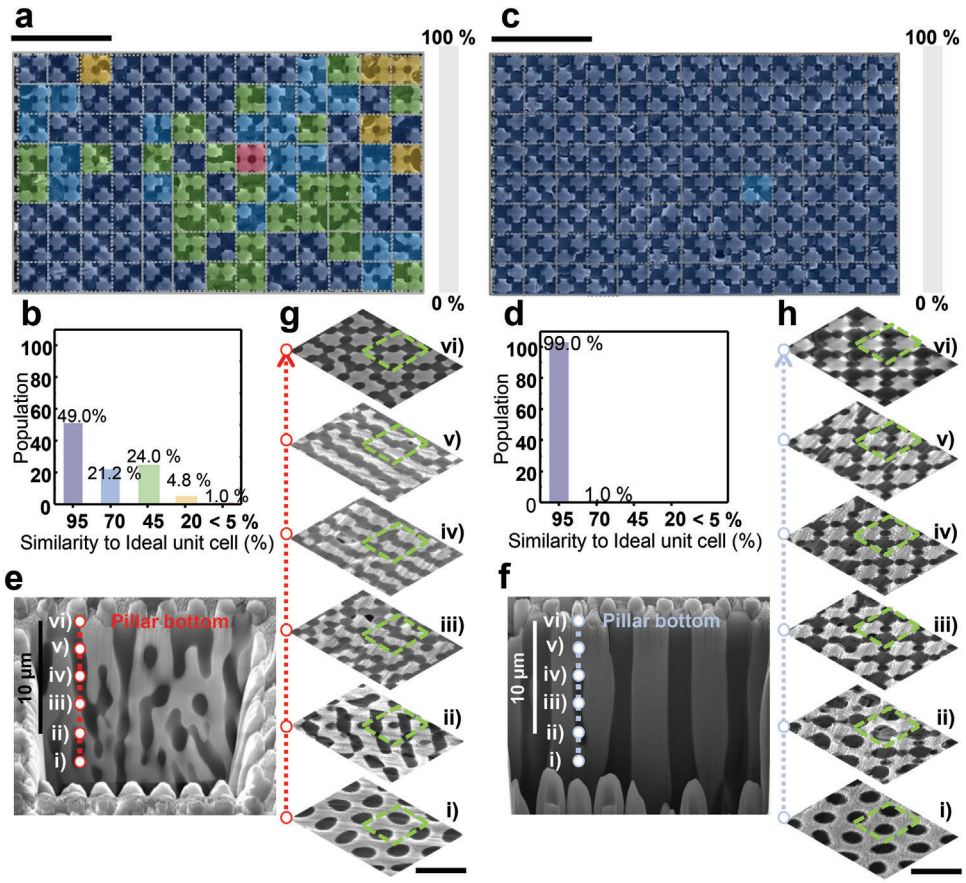

Figure 4. 3D microstructure of the eutectic grown in Si and pSi templates and image analysis of patterns (n = 104). a,c) Checkerboard patterns at the substrate/template interface generated by (a) the high thermal conductivity Si template and c) the low thermal conductivity pSi template (scale bar for both: 20 µm). Image analysis of checkerboard pattern where the color of unit cell indicates similarity to an ideal unit cell (navy color (100% similarity). b,d) Histogram from image analysis of (b) and (d) representing the number of unit cells in which the indicated degree of similarity to the ideal unit cell. e,f) SEM images of a FIB prepared cross-section of template-directed solidified AgCl and KCl for the e) Si pillar and f) pSi pillar templates. g,h) SEM images of (e) and (f) at every 2.5 µm in depth (vi through i) (scale bar is 5 µm); the unit cell is represented by the green dashed box.

Figure 4gv, shows the lamellar pattern (which in the template develops a spoke pattern) transitioning to defected structures. Overall, the resulting structures are irregularly formed spokes or exhibit a defective checkerboard pattern during the intermediate stage of solidification, which we attribute to non-planar solidification front and the presence of horizontal components in the temperature gradient, as discussed above. Finally, the checkerboard and spokes patterns are arranged in an irregular manner at the template/substrate interface (Figure 4gvi). These results contrast with the structure observed in serial sectioning of the checkerboard pattern formed by the pSi template (Figure 4h; see Figure S12b, Supporting Information). In the pSi structure, a single morphology is maintained during solidification through the template. Starting from the bulk rod structure (Figure 4hi), the rod structures are maintained at the bulk-eutectic/template interface, and their hexagonal arrangement traverses into the spaces between the pillars (ii and iii, Figure 4hii,iii) to the bottom of the template (Figure 4hiv,v,vi), strong evidence that the solidification front remains flat as it traverses through the template.

2.4. Optical Properties

In our exploration of templated eutectic systems, we utilize etching techniques to selectively remove one or more phases from the templated eutectic to tune the properties of the eutectic structures, as has been done for different applications of eutectic materials including differentially wettable surfaces,[50] sensors,[51] and batteries.[52] In the systems reported here, the optical contrast can be enhanced by selective etching of one or two of the phases. As grown, the templated eutectic structures exhibit an optical response because the pillars, the KCl, and AgCl all have different refractive indices. Because KCl is easily dissolved by water and AgCl is not, the refractive index variations within the structure, and thus the optical response, can be modified via a simple water etching step. The result of water etching is a AgCl/pillar microstructure with voids in place of KCl (Figure S13, Supporting Information). Alternatively, the pSi (or Si) templates can be selectively removed by XeF_2 gas, and/or the AgCl converted to porous Ag metal by UV light (**Figure 5a–d**). Consequently, from a single templated eutectic structure, it is possible to create a range of

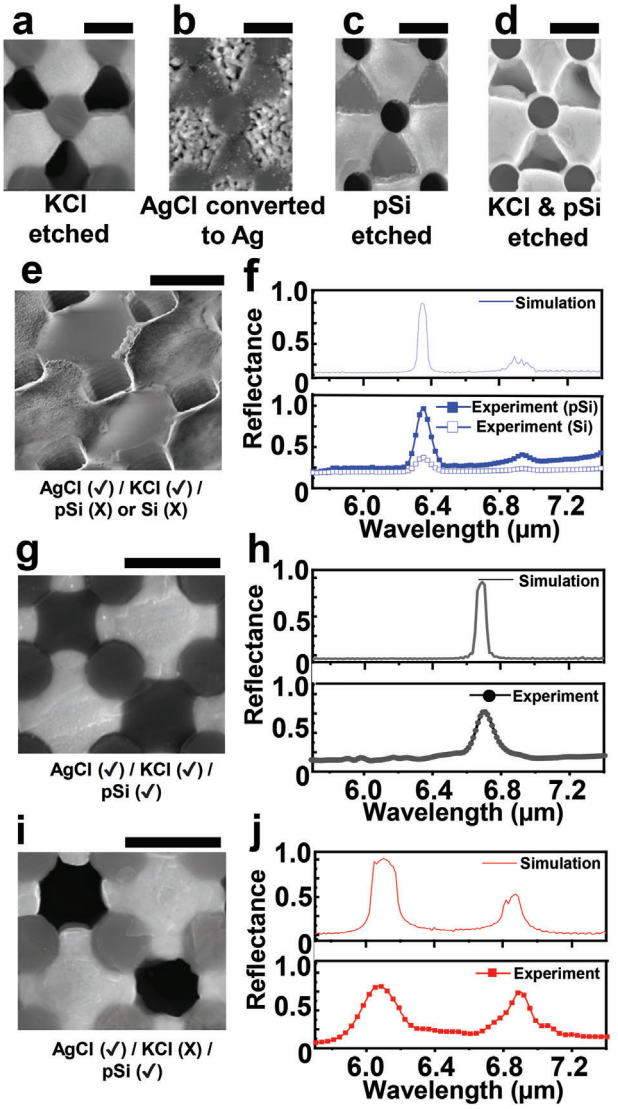

Figure 5. Microstructure and photonic properties of ordered and disordered checkerboard patterns before and after selective etching/materials conversion. a-d) SEM images of ordered checkerboard patterns after, a) etching of KCl by water, b) conversion of AgCl to Ag metal by UV light, c) etching of pSi by XeF_2 gas and d) etching of pSi and KCl by XeF_2 gas and water (scale bars are 3 μm). e) SEM image of checkerboard pattern after etching of pillar template and f) reflectance spectra of eutectic templated by pSi (filled squares) and Si (open squares), and FDTD simulated spectrum for an idealized structure. SEM images of checkerboard pattern, g) before and i) after KCl etching (scale bar is 3 μm). h,j) Reflectance spectra and the FDTD simulation for idealized structure, h) before KCl etching and, j) After KCl etching.

dielectric and metallo-dielectric 2D photonic crystals, expanding upon the scope of dielectric 2D photonic crystals derived from eutectic systems.[10,24,28] Optical spectroscopy is performed on several of this family of structures. As a first step, the bulk eutectic above the pillars is removed by mechanical and ion beam polishing. Then, normal incidence reflectance spectra are taken using a Fourier-transform infrared (FTIR) microscope and compared to finite-difference time domain (FDTD) simulations. Figure 5f shows that the reflectance spectrum of the checkerboard pattern (pSi or Si pillars etched, Figure 5e) is expected to exhibit two distinct peaks at 6.37 and 6.88 μm based on the FDTD simulation. The well-ordered microstructure made via the pSi template shows the expected peaks whereas the microstructure resulting from the Si template did not (Figure 5f). In a pSi-templated sample containing all three components, pSi pillars, AgCl, and KCl (Figure 5g), the measured reflectance peak at 6.67 μm corresponds well with the FDTD simulations (Figure 4h). When KCl is etched from this sample (Figure 5i), peaks are observed at 6.12 and 6.88 μm, in agreement with the FDTD simulation (Figure 5j). The optical properties after removal of both the pillars and KCl (leaving only AgCl) is investigated by FDTD simulation, revealing broad peaks ≈5.9 and 6.5 μm (Figure S14, Supporting Information) although such a sample was not experimentally examined. By comparing this simulation with the simulation in Figure 5j corresponding to the sample where only KCl is removed, it is shown that the pSi pillars cause only a slight red shift of the 6.88 and 6.12 μm peaks in Figure 5j. As the refractive index of pSi is only ≈1.2,[39] it is not surprising that the effect of the pillars on optical properties is modest. As a general comment, the optical properties of inorganic eutectic phases can be manipulated over a wider range than possible in organic systems where most refractive indices are similar. We envision that the roadmap for forming highly regular eutectic structures via template-directed self-assembly presented here will lead to new opportunities for developing improved materials, especially in optics, which benefit from highly regular microstructures. The fundamental principles discussed here, which guide the design of templates for generating highly periodic eutectic microstructures, may be important for a diverse set of self-assembling materials beyond those based on eutectic solidification, potentially leading to new classes of materials with as yet unrealized properties and functionalities.

3. Conclusions

Thermal engineering of the template is found to significantly improve both the short- and long-range order of mesostructures that result from template-directed eutectic solidification. Our findings clarify the interplay between the thermal characteristics of the eutectic and the template, along with the template geometry, that determines the resulting mesostructure. Simulations indicate that the use of a template with low thermal conductivity offered significant advantages for achieving unidirectional solidification in the context of template-directed solidification. As an example of the use of a low thermal conductivity template, here, pSi with $\kappa \approx 0.28\ Wm^{-1}K^{-1}$ and thermal diffusivity ≈0.89 mm^2/s is utilized as the template material. This thermally engineered template-guided eutectic solidification results in highly regular and periodic mesostructures with 99% of the mesostructure having a pattern similar to the ideal unit cell. The 3D structure of the eutectic solidified into the template is investigated, and the mesostructure is determined to be very well-preserved within the template and without a sign of undesirable morphological transitions during solidification. The optical properties of the structures formed using the thermally engineered template are found to match simulations of an ordered structure, while the optical properties of structures formed using a high-thermal-conductivity template do not. We note that the optical properties

can be tuned by selectively etching one or more components in the structure.

4. Experimental Section

Fabrication of pSi Pillar Template: The pSi pillar arrays were fabricated using p-type silicon wafers (Prolog, boron doped, 0.001 Ω cm resistivity, (100)-orientation). Circular dots (2 µm in diameter) in square or hexagonal arrays with 1.4, 1.8 or 2.2 µm pillar edge to pillar edge gaps (g) are patterned by photolithography with SPR220 (Dow chemical), and directly utilized as etching masks. Then, the photoresist patterned Si is etched by deep-reactive ion etching (DRIE) (STS Pegasus). The DRIE process is carried out using SF_6 (390 sccm)/C_4F_8 (250 sccm) in cyclic etching mode and passivation with a 3000 W source power, using 30 mTorr gas pressure. These Si pillar arrays are used as a template. To porosity the Si pillars, hydrofluoric acid based electrochemical etching is carried out.[39] A silicon pillar array is placed in a polypropylene cell with an exposed area of ≈1.2 cm^2 and the back side of the silicon is in contact with a stainless-steel electrode. A 5 mm diameter Pt–Ir inoculating loop was placed 2.5 cm above the silicon as a counter electrode. The sample is submerged in an electrolyte composed of a 1:1.48 volume ratio of 100% ethanol and aqueous 48% hydrofluoric acid. An SP-200 potentiostat (BioLogic Science Instruments) delivers current to the wafer at a current density of 400 mA cm^{-2} to porosify the silicon in the exposed region. After etching, the samples are thoroughly rinsed with ethanol, followed by supercritical drying using a critical point dryer (Autosamdri 931). After porosification, the template is conformally coated with 20 nm of Al_2O_3 by atomic layer deposition (Savannah S100 Cambridge Nanotech).

Eutectic Solidification into Pillar Templates: AgCl (99.999%, Sigma Aldrich) and KCl (99.99%, Sigma Aldrich) were mixed with eutectic composition of 81.77 wt.% AgCl and 18.23 wt.% KCl, completely melted in a glass vial on a hotplate at 450 °C for 3 h and allowed to cool to room temperature. Eutectic solidification into Si and pSi pillar templates was performed with a Linkam THMS 600 hot-stage (with a TMS 94 controller). The set-up for directional solidification is designed to minimize uncontrollable heat conduction, convection, or radiation, as schematically described in Figure S3 (Supporting Information). A 2 mm on a side cube of pre-solidified AgCl-KCl was prepared using a Princeton WS-25 wire saw, and then placed on the top of the template (Figure S3a, Supporting Information). Subsequently, Si spacers are placed onto the edge of the pillar templates with the cube of pre-solidified bulk eutectic (≈200 mg) in the center of the template. The bulk eutectic and Si spacers are covered with a glass slide and heated to 430 °C for 10 min until the eutectic completely melted and fully wet the template (Figure S3b, Supporting Information). The melted and infilled eutectic into templates was cooled to room temperature with controlled cooling rates from 1 °C/min to 40 °C/min, driving solidification parallel to the pillars of the template (Figure S3c, Supporting Information).

Microstructure Characterization and Ion Beam Etching: After peeling off the template substrate, the bottom of the sample composed of the Si or pSi pilar array, AgCl, and KCl was imaged by focused ion beam scanning electron microscopy (FIB-SEM) (Scios 2, Thermo Fisher Scientific). For cross-section imaging Ga FIB milling (15 nA, 30 kV) is used. After that, the cross-section is cleaned at 3 nA and 30 kV. For serial cross-section imaging, samples are etched by an argon ion polishing system (PECS II, Gatan, Inc.). Before ion beam etching of the samples, rectangular marks are formed by FIB at each corner of the designated area for imaging. After taking an image of the designated area, the sample is etched at 6 keV for 30 min (etch rate of 0.08 µm/min). Through repetitive etching and imaging, the serial-sectioning images are obtained.

Thermal Property Measurement: κ of a 5 µm thick film of pSi and a boron-doped Si wafer is measured by the differential 3-omega method[53] at room temperature. An insulating 1 µm SiO_2 layer was insulated by plasma-enhanced chemical vapor deposition (Oxford PlasmaPro 100) on the sample. Four-point resistive thermometer sensors with dimensions 1.5 mm long, 200 nm thick and ≈100 µm wide were patterned by e-beam evaporation of gold through a shadow mask. Sensors were electrically connected to a chip carrier by ball bonding or silver epoxy. The sensor was calibrated by changing temperature and measuring resistance on a temperature-controlled plate. To conduct the 3-omega measurement, an SR 830 digital lock-in amplifier provided a sinusoidal voltage source across the thermometers and detected voltages at the 3rd harmonic of the input source. AC current is measured by placing a digital multi-meter (Agilent 34401A) in series with the circuit before and after measurement. A common-mode subtraction circuit containing a manual trimpot is employed to reduce the 1-omega component of the signal. To determine the heat capacities of Si and pSi, a small piece of Si wafer weighing ≈15 mg was employed for measurement. In the case of pSi, the pSi membrane was carefully transferred to DSC pans to facilitate accurate heat capacity measurements.

Thermal Profile Calculations: Heat transfer simulations were performed using COMSOL Multiphysics to examine the shape of the solidification front as it traverses across the Si pillars. The model geometry, from top to bottom, consists of a 0.17 mm long glass, a 0.3 mm long layer of AgCl-KCl, a unit cell of Si pillars (each with radius of 1 µm and length of 10 µm) arranged in a square array, and a 0.3 mm long Si substrate. Neumann boundary conditions for Newton's law of cooling were applied to upward-facing horizontal surfaces of the silica glass. For the cooling case, the air temperatures were initially 400 °C and decreased at a rate of 2 °C min^{-1}. The temperature profiles for eutectic and spacings between template were calculated as a function of time by solving the heat equation, and the solidification positions were approximated by the isocontour at the eutectic temperature (591.73 K). Further details are provided in Supporting Information.

Optical Characterization and Optical Simulation: Reflection spectra were collected from a 20 µm diameter spot on the sample using a FTIR microscope (Vertex 70 FTIR and Bruker hyperion microscope). For optical characterization, the bulk eutectic beneath the templated patterns was removed by mechanical polishing and ion polishing. Incident light was perpendicular to the pillar axis. An unpolarized globar light source and a CaF_2 beam splitter were used. A silver mirror was used as a reference. ANSYS Lumerical Software ULC with FDTD solver (version 8.27.3044) was used to simulate the reflectance spectra. SEM images provided the necessary parameters for pillar diameter and spacing and AgCl-KCl distribution in the pattern to design the simulation model. Fixed refractive indices were used for pSi (1.2), silicon (3.5), AgCl (2.01), and KCl (1.48) and all materials were treated as lossless. A square unit cell was designed with a lattice constant of 3.5 µm and pillar diameter of 2.25 µm, and 128 layers of pillars were used to simulate the spectra shown in Figure 4. The reflectance spectra were simulated with and without KCl. Standard perfectly matched layer boundary conditions were used for the simulations and reflection spectra were recorded along the direction perpendicular to the axis of the pillars.

Image Analysis and Statistical Analysis: The image analysis process was executed using a script crafted for FIJI/ImageJ software, version 1.53p.[54] The initial step in image analysis involved adjusting the raw SEM images to reduce large-scale background variation using a pseudo-flat field correction with a 50-pixel radius. This was essential for preparing the SEM images for detailed analysis. After pre-processing, the full-view micrographs were rotated as necessary to align the supercell patterns with the image grid. The images were then trimmed to include a complete number of cells in both the x and y directions. For the statistical analysis, a total of 104 supercells were evaluated to quantify the long-range ordering patterns within the material being studied. Cropped images were first divided into a stack of supercell "tiles." To address the possibility of tiles displaying the ideal supercell pattern but flipped across the center, each tile is split into four quadrants. The tiles are then binarized to differentiate materials—such as white for AgCl and black for KCl—using an automatic intensity threshold determined by the "triangle" method.[55] The deviation of each tile from the ideal pattern was evaluated by comparing the fraction of pixels that differ from a binary ideal supercell pattern set on the same pixel grid, where the pixel size varies based on the original image. This data was also used to create a color overlay that visualizes the deviation of each tile.

Supporting Information

Supporting Information is available from the Wiley Online Library or from the author.

Acknowledgements

This work was primarily supported by the Army Research Office (MURI Grant No. W911NF-17-1-0351). KT and GH acknowledge support of GENESIS: A Next Generation Synthesis Center, an Energy Frontier Research Center funded by the US Department of Energy (DOE), Office of Science, Basic Energy Sciences under award No. DE-SC0019212.

Conflict of Interest

The authors declare no conflict of interest.

Data Availability Statement

The data that support the findings of this study are available from the corresponding author upon reasonable request.

Keywords

complex mesostructures, eutectic solidification, photonics, template-directed self-assembly, thermal engineering

Received: August 27, 2023
Revised: January 3, 2024
Published online:

[1] C. Bae, H. Yoo, S. Kim, K. Lee, J. Kim, M. M. Sung, H. Shin, *Chem. Mater.* **2008**, *20*, 756.
[2] E. Mohammadi, C. Zhao, Y. Meng, G. Qu, F. Zhang, X. Zhao, J. Mei, J.-M. Zuo, D. Shukla, Y. Diao, *Nat. Commun.* **2017**, *8*, 16070.
[3] E. M. Pouget, P. H. H. Bomans, J. A. C. M. Goos, P. M. Frederik, G. De With, N. A. J. M. Sommerdijk, *Science* **2009**, *323*, 1455.
[4] J. A. Swift, A. M. Pivovar, A. M. Reynolds, M. D. Ward, *J. Am. Chem. Soc.* **1998**, *120*, 5887.
[5] Y. Xia, P. Yang, *Adv. Mater.* **2003**, *15*, 351.
[6] L. Zhang, G. M. Biesold, C. Y. Zhao, H. Xu, Z. Q. Lin, *Adv. Mater.* **2022**, *34*, 30.
[7] J. Z. Zhou, X. Wu, Y. Chen, C. Yang, R. Yang, J. Y. Tan, Y. L. Liu, L. Qiu, H. M. Cheng, *Adv. Funct. Mater.* **2022**, *32*, 8.
[8] Z. Jiang, J. H. Pikul, *Nat. Mater.* **2021**, *20*, 1512.
[9] K. Hofhuis, S. H. Skjærvø, S. Parchenko, H. Arava, Z. Luo, A. Kleibert, P. M. Derlet, L. J. Heyderman, *Nat. Phys.* **2022**, *18*, 699.
[10] J. Kim, L. K. Aagesen, J. H. Choi, J. Choi, H. S. Kim, J. Liu, C.-R. Cho, J. G. Kang, A. Ramazani, K. Thornton, P. V. Braun, *Adv. Mater.* **2015**, *27*, 4551.
[11] L. Ran, S. Qiu, P. Zhai, Z. Li, J. Gao, X. Zhang, B. Zhang, C. Wang, L. Sun, J. Hou, *J. Am. Chem. Soc.* **2021**, *143*, 7402.
[12] Y. Ding, K. R. Gadelrab, K. Mizrahi Rodriguez, H. Huang, C. A. Ross, A. Alexander-Katz, *Nat. Commun.* **2019**, *10*, 2974.
[13] G. S. Doerk, K. G. Yager, *Mol. Syst. Des. Eng.* **2017**, *2*, 518.
[14] C. G. Hardy, C. Tang, *J. Polym. Sci., Part B: Polym. Phys.* **2013**, *51*, 2.
[15] M. P. Stoykovich, M. MuLler, S. O. Kim, H. H. Solak, E. W. Edwards, J. J. De Pablo, P. F. Nealey, *Science* **2005**, *308*, 1442.
[16] A. A. Kulkarni, E. Hanson, R. Zhang, K. Thornton, P. V. Braun, *Nature* **2020**, *577*, 355.
[17] S. Akamatsu, M. Plapp, *Curr. Opin. Solid State Mater. Sci* **2016**, *20*, 46.
[18] M. G. Blaber, C. J. Engel, S. R. C. Vivekchand, S. M. Lubin, T. W. Odom, G. C. Schatz, *Nano Lett.* **2012**, *12*, 5275.
[19] R. Deska, K. Sadecka, J. Olesiak-Banska, K. Matczyszyn, D. A. Pawlak, M. Samoc, *Appl. Phys. Lett.* **2017**, *110*, 031102.
[20] K. Sadecka, M. Gajc, K. Orlinski, H. B. Surma, A. Klos, I. Jozwik-Biala, K. Sobczak, P. Dluzewski, J. Toudert, D. A. Pawlak, *Adv. Opt. Mater.* **2015**, *3*, 381.
[21] J. Tang, R. Daiyan, M. B. Ghasemian, S. A. Idrus-Saidi, A. Zavabeti, T. Daeneke, J. Yang, P. Koshy, S. Cheong, R. D. Tilley, R. B. Kaner, R. Amal, K. Kalantar-Zadeh, *Nat. Commun.* **2019**, *10*, 4645.
[22] S. Zhu, H. Akamine, Y. Nagahata, T. Tojigamori, H. Miki, Y. Zhang, T. Tokunaga, S. Iikubo, *J. Alloys Compd.* **2023**, *930*, 167447.
[23] Z. Zhao, S. Soni, T. Lee, C. A. Nijhuis, D. Xiang, *Adv. Mater.* **2023**, *35*, 2203391.
[24] J. Choi, A. A. Kulkarni, E. Hanson, D. Bacon-Brown, K. Thornton, P. V. Braun, *Adv. Opt. Mater.* **2018**, *6*, 1701316.
[25] M. Perrut, A. Parisi, S. Akamatsu, S. Bottin-Rousseau, G. Faivre, M. Plapp, *Acta Mater.* **2010**, *58*, 1761.
[26] M. Perrut, S. Akamatsu, S. Bottin-Rousseau, G. Faivre, *Phys. Rev. E* **2009**, *79*, 032602.
[27] J. Tang, S. Lambie, N. Meftahi, A. J. Christofferson, J. Yang, J. Han, M. A. Rahim, M. Mayyas, M. B. Ghasemian, F.-M. Allioux, Z. Cao, T. Daeneke, C. F. Mcconville, K. G. Steenbergen, R. B. Kaner, S. P. Russo, N. Gaston, K. Kalantar-Zadeh, *Nat. Synth.* **2022**, *1*, 158.
[28] A. A. Kulkarni, J. Kohanek, E. Hanson, K. Thornton, P. V. Braun, *Acta Mater.* **2019**, *166*, 715.
[29] A. A. Kulkarni, J. Kohanek, K. I. Tyler, E. Hanson, D.-U. Kim, K. Thornton, P. V. Braun, *Adv. Opt. Mater.* **2018**, *6*, 1800071.
[30] Z. Yan, M. D. Han, Y. Shi, A. Badea, Y. Y. Yang, A. Kulkarni, E. Hanson, M. E. Kandel, X. W. Wen, F. Zhang, Y. Y. Luo, Q. Lin, H. Zhang, X. G. Guo, Y. M. Huang, K. W. Nan, S. Jia, A. W. Oraham, M. B. Mevis, J. M. Lim, X. L. Guo, M. Y. Gao, W. Ryu, K. J. Yu, B. G. Nicolau, A. Petronico, S. S. Rubakhin, J. Lou, P. M. Ajayan, K. Thornton, et al., *Proc. Natl. Acad. Sci. USA* **2017**, *114*, E9455.
[31] D. A. Pawlak, S. Turczynski, M. Gajc, K. Kolodziejak, R. Diduszko, K. Rozniatowski, J. Smalc, I. Vendik, *Adv. Funct. Mater.* **2010**, *20*, 1116.
[32] A. M. Urbas, Z. Jacob, L. D. Negro, N. Engheta, A. D. Boardman, P. Egan, A. B. Khanikaev, V. Menon, M. Ferrera, N. Kinsey, C. Devault, J. Kim, V. Shalaev, A. Boltasseva, J. Valentine, C. Pfeiffer, A. Grbic, E. Narimanov, L. Zhu, S. Fan, A. Alù, E. Poutrina, N. M. Litchinitser, M. A. Noginov, K. F. Macdonald, E. Plum, X. Liu, P. F. Nealey, C. R. Kagan, C. B. Murray, et al., *J. Opt.* **2016**, *18*, 093005.
[33] E. Hanson, *Doctoral thesis*, University of Michigan **2019**.
[34] H. R. Shanks, P. D. Maycock, P. H. Sidles, G. C. Danielson, *Phys. Rev.* **1963**, *130*, 1743.
[35] D. Li, Y. Wu, P. Kim, L. Shi, P. Yang, A. Majumdar, *Appl. Phys. Lett.* **2003**, *83*, 2934.
[36] W. Liang, G. Lu, J. Yu, *Adv. Theory Simul.* **2022**, *5*, 2200206.
[37] I. K. Mamedov, D. G. Arasly, A. A. Khalilova, R. N. Rahimov, *Inorg. Mater.* **2019**, *55*, 320.
[38] I. Manasijevic, L. Balanovic, D. Minic, M. Gorgievski, U. Stamenkovic, *Kovove Mater.* **2019**, *57*, 267.
[39] T. Wang, S. Viswanathan, D. Mantha, R. G. Reddy, *Sol. Energy Mater. Sol. Cells* **2012**, *102*, 201.
[40] G. Amato, R. Angelucci, G. Benedetto, L. Boarino, L. Dori, P. Maccagnani, A. M. Rossi, R. Spagnolo, *J. Porous Mater.* **2000**, *7*, 183.
[41] S. Erfantalab, G. Parish, A. Keating, *Int. J. Heat Mass Transfer* **2022**, *184*, 122346.
[42] F. Lucklum, A. Schwaiger, B. Jakoby, *Sens. Actuators, A* **2014**, *213*, 35.
[43] V. Lysenko, V. Gliba, V. Strikha, A. Dittmar, G. Delhomme, P. Roussel, D. Barbier, N. Jaffrezic-Renault, C. Martelet, *Appl. Surf. Sci.* **1998**, *123*, 458.

[44] N. A. Krueger, A. L. Holsteen, S.-K. Kang, C. R. Ocier, W. Zhou, G. Mensing, J. A. Rogers, M. L. Brongersma, P. V. Braun, *Nano Lett.* **2016**, *16*, 7402.
[45] M. Asheghi, K. Kurabayashi, R. Kasnavi, K. E. Goodson, *J. Appl. Phys.* **2002**, *91*, 5079.
[46] N. Chakraborty, *Appl. Therm. Eng.* **2009**, *29*, 3618.
[47] P. I. Nabelek, A. M. Hofmeister, A. G. Whittington, *Earth Planet. Sci. Lett.* **2012**, *317*, 157.
[48] G. Pottlacher, H. Hosaeus, E. Kaschnitz, A. Seifter, *Scand. J. Metall.* **2002**, *31*, 161.
[49] A. I. Persson, Y. K. Koh, D. G. Cahill, L. Samuelson, H. Linke, *Nano Lett.* **2009**, *9*, 4484.
[50] K. Z. Hossain, M. Monwar, M. R. Khan, *Soft Matter* **2023**, *19*, 3199.
[51] J. Tang, S. Lambie, N. Meftahi, A. J. Christofferson, J. Yang, M. B. Ghasemian, J. Han, F.-M. Allioux, M. A. Rahim, M. Mayyas, T. Daeneke, C. F. Mcconville, K. G. Steenbergen, R. B. Kaner, S. P. Russo, N. Gaston, K. Kalantar-Zadeh, *Nat. Nanotechnol.* **2021**, *16*, 431.
[52] M. Zhang, R. Liang, N. Yang, R. Gao, Y. Zheng, Y.-P. Deng, Y. Hu, A. Yu, Z. Chen, *Adv. Energy Mater.* **2022**, *12*, 2102493.
[53] D. G. Cahill, M. Katiyar, J. R. Abelson, *Phys. Rev. B* **1994**, *50*, 6077.
[54] G. W. Zack, W. E. Rogers, S. A. Latt, *J. Histochem. Cytochem.* **1977**, *25*, 741.
[55] J. Schindelin, I. Arganda-Carreras, E. Frise, V. Kaynig, M. Longair, T. Pietzsch, S. Preibisch, C. Rueden, S. Saalfeld, B. Schmid, J.-Y. Tinevez, D. J. White, V. Hartenstein, K. Eliceiri, P. Tomancak, A. Cardona, *Nat. Methods* **2012**, *9*, 676.